Mechanism and Machine Theory 173 (2022) 104863

Contents lists available at ScienceDirect

Mechanism and Machine Theory

journal homepage: www.elsevier.com/locate/mechmt

Research paper

A robotic surgical tool with continuum wrist, kinematically optimized curved stem, and collision avoidance kinematics for single port procedure

Zhonghao Wu [a], Chuanxiang Zhu [b], Yue Ding [b], Yifan Wang [b], Bin Xu [c], Kai Xu [b,*]

[a] UM-SJTU Joint Institute, Shanghai Jiao Tong University, Shanghai 200240, China
[b] School of Mechanical Engineering, Shanghai Jiao Tong University, Shanghai 200240, China
[c] Department of Urology, Shanghai Ninth People's Hospital, Shanghai Jiao Tong University School of Medicine, Shanghai 200011, China

ARTICLE INFO

Keywords:
Collision Avoidance
Continuum Mechanism
Structural Parameter Optimization
Single Port Laparoscopy
Surgical Robots

ABSTRACT

Robot-assisted minimally invasive key-hole surgeries have thrived in recent decades, primarily robotic MPL (Multi-Port Laparoscopy) and SPL (Single Port Laparoscopy). In robotic MPL, surgical manipulators are mainly equipped with straight-stemmed tools with distal wrists. For robotic SPL, when these MPL tools and manipulators are used via a single entry, they often suffer from mutual collisions. On the other hand, dedicated SPL manipulators/tools usually lack adequate payload capabilities due to the slim multi-joint designs. To facilitate SPL, a SORST (Stem-Optimized Robotic Surgical Tool) with a continuum wrist and a kinematically optimized rigid curved stem is proposed. The SORST's curved but rigid stem can help reduce possible collisions and maintain the tool's payload capability. In this curved-stem tool, the tendon tension might be difficult to properly maintain, due to the fact that the tendon may get in contact with the guiding cannula with uncertain friction. Hence, the continuum wrist is introduced for enhancing distal dexterity. Furthermore, an instantaneous inverse kinematics framework is proposed to simultaneously avoid mutual collisions and satisfy the remote-center-of-motion constraint, joint range/velocity limits, and the desired task space twist. Extensive experimental verifications were conducted to demonstrate the efficacy.

1. Introduction

Robot-assisted minimally invasive key-hole surgeries, primarily robotic MPL (Multi-Port Laparoscopy) and SPL (Single Port Laparoscopy), have thrived in recent decades, providing patients lower pain, faster recovery, etc. [1].

In robotic MPL, multiple surgical tools are usually maneuvered by several patient-side manipulators next to a surgical bed through several access ports in a patient's abdominal wall. The surgical tools often have a straight stem to generate a large translational workspace and a distal wrist to enhance distal dexterity (the capability of orienting the surgical end effector) [2]. Existing investigations often focus on distal dexterity enhancement [3], force-sensing capability [4], manipulator topology deployment, such as RCM (Remote-Center-of-Motion) mechanism designs [5], etc.

Because these MPL manipulators have an articulated structure, active investigations include i) inverse kinematics solutions for

---

* Corresponding author at: Shanghai Jiao Tong University, School of Mechanical Engineering, Shanghai 200240, China.
E-mail address: k.xu@sjtu.edu.cn (K. Xu).

https://doi.org/10.1016/j.mechmachtheory.2022.104863
Received 14 November 2021; Received in revised form 5 March 2022; Accepted 24 March 2022

handling the RCM constraint [6–8], ii) joint constraint handling [9], iii) surgical port placement optimization [10–12], and iv) instrument collision avoidance via null space projection [13] or virtual fixtures [14–16].

To benefit patients with further reduced trauma and improved recovery, robotic SPL has started to gain popularity. However, directly applying the MPL tools and manipulators for SPL paradigms via a single abdominal entry may lead to high risks of mutual collisions between the crowdedly deployed manipulators and tools. On the other hand, dedicated SPL tools with slim multi-joint designs may suffer from inadequate payload capabilities, due to the size limitation from the diameters of the deployment channels, even though the collision risks of the tools' actuation are usually mitigated by the SPL robots' system designs. Existing studies on SPL robots are all centered around the compromise between sufficient kinematic performance and adequate payload capability, regardless of using either cable actuation [17], embedded motors [18], linkage-based transmission [19], or continuum mechanisms [20].

Among the MPL and SPL manipulator designs, continuum manipulators have received considerable attention, due to their design compactness, dexterity, intrinsic compliance, etc. The kinematics of the continuum robotic tools can be formulated by Hamilton's principle [21], elliptic integrals [22], Cosserat-rod theory [23], or the principle of virtual power [24, 25]. For the purposes of model simplicity and real-time calculation/control, the kinematics based on the constant curvature bending assumption is widely adopted [26].

To maintain sufficient distal dexterity and payload capability, and decrease mutual collision risks between the patient-side extracorporeal manipulators, a SORST (Stem-Optimized Robotic Surgical Tool) with a kinematically optimized rigid curved stem and a continuum wrist is proposed for a single port procedure, as shown in Fig. 1. The comparison between the proposed SORST and the existing tool with a rigid straight stem [27] is shown in Fig. 1(c). Because a rigid (although curved) stem is still used, the payload capability is thus kept at an adequate level. If a tendon-driven wrist is integrated at the distal end, it will be challenging to maintain proper tensions on the actuation tendons when the tendons are routed inside the curved stem. Therefore, a multi-backbone continuum wrist is integrated for distal dexterity enhancement. To the best of the authors' knowledge, SORST is the first to use a kinematically optimized rigid curved stem to further enhance the end effector dexterity, to help reduce possible mutual collisions. Among the existing systems, only the da Vinci Single-Site$^{\mathrm{TM}}$ instrument has a non-fully straight stem. However, the Single-Site$^{\mathrm{TM}}$ tools are maneuvered by a parallelogram-based mechanical RCM mechanism, and the RCM point is constrained along the stem's straight portion. The stem's curved portion is not exploited to enhance distal dexterity. In contrast, the curved shape of the SORST stem is intentionally utilized to enhance distal dexterity.

When the SORSTs are deployed and maneuvered by patient-side manipulators through an abdominal entry under a compact SPL deployment, mutual collisions between the manipulator-SORST systems are more likely to occur. However, the collision avoidance approaches in MPL deployment mainly focus on avoiding collisions between extracorporeal manipulators. For manipulator-SORST systems, both extracorporeal manipulators and intracorporeal curved stems should be considered. Moreover, the existing methods [6–8] for satisfying the RCM constraint cannot handle the curved stem of SORST. Therefore, an instantaneous inverse kinematics framework for the SORST tool is proposed to match the desired task space twist and satisfy the joint range/velocity limits, the RCM constraint along the curved stem, and the collision avoidance in a prioritized manner.

The contributions of this paper can be summarized as follows.

- A robotic surgical tool with a kinematically optimized curved (but rigid) stem and a multi-backbone continuum wrist is proposed to enhance distal dexterity in a confined surgical site and maintain adequate payload capability;

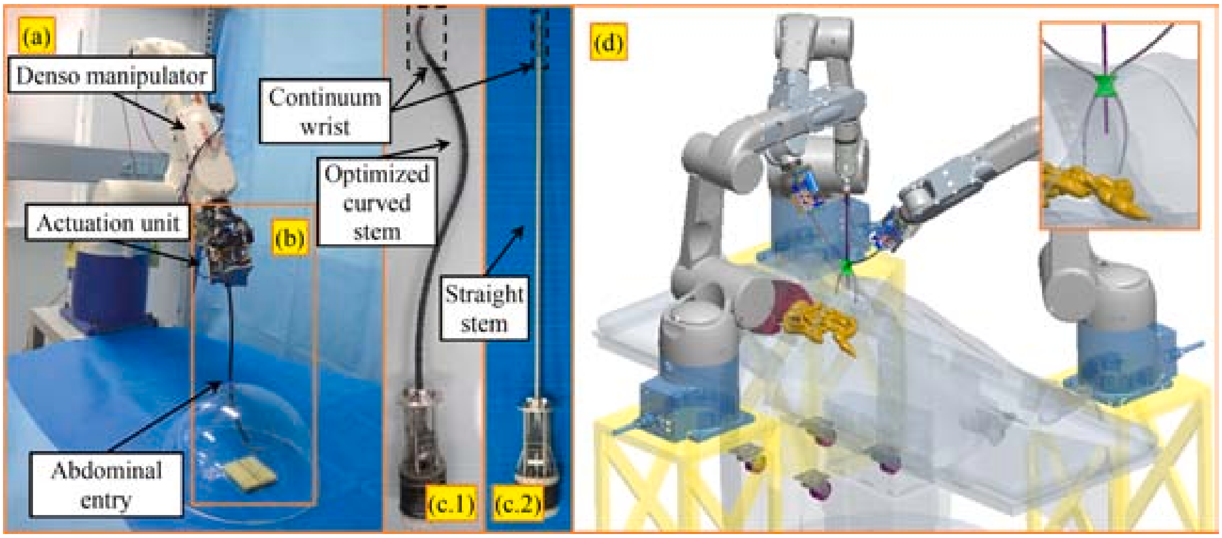

Fig. 1. (a) The proposed SORST, with an optimized curved stem and a multi-backbone continuum wrist attached to the distal end of a Denso manipulator, (b) the SORST and its actuation unit, (c.1&c.2) the exchangeable surgical tool with a curved stem for SPL (SORST), and with a straight stem for MPL [27], (d) deployment of the manipulator-SORST systems for SPL.

- A prioritized inverse kinematics framework is proposed for the manipulator-SORST system to handle the desired task space twist, the joint range/velocity limits, the RCM constraint, and the mutual collision avoidance constraint.
- Simulations and experimental characterizations of the manipulator-SORST systems are presented to show the effectiveness of the proposed design and kinematics framework.

The remainder of the paper is organized as follows. Section 2 introduces the design overview and the manipulator-SORST system. Section 3 presents the nomenclature and the kinematics derivation necessary for the prioritized inverse kinematics framework that is elaborated in Section 4. Dexterity analysis and kinematic optimization of the SORST curved stem are reported in Section 5, with the experimental characterizations reported in Section 6. The conclusion and future work are summarized in Section 7.

2. Design overview and system descriptions

The SORST for SPL is designed to have a curved stem and 2-DoF (Degree of Freedom) continuum wrist for improved distal dexterity and adequate payload capability. During possible surgical use, it will be attached to a general manipulator to perform basic surgical tasks via a single incision in a patient's abdominal wall.

A Denso manipulator is selected to maneuver the SORST, due to the availability of the Denso's control interface for real-time path planning capability.

The SORST is described in Section 2.1, while the SORST actuation unit and the control infrastructure are briefly recalled in Section 3.2.

2.1. *The SORST tool*

As a proof-of-concept, the SORST tool for SPL is shown in Fig. 2, consisting of five main components: i) an end effector (a gripper is integrated as an example), ii) a distal segment as a dexterous continuum wrist, iii) a curved stem, iv) several guiding channels, and v) a proximal segment. The abovementioned five components are listed from the distal end to the proximal end, referring to Fig. 2.

The distal and proximal segments are structurally similar to those shown in Fig. 3(b). Each of the segments includes a base ring, several spacer rings (or two bellows in the distal segment), an end ring, and multiple backbones. The segments are bent by pulling and pushing these backbones that are made of super-elastic nitinol. The spacer rings (or the bellows in the distal segment) can prevent buckling of the backbones under compressive loads. The segments' bent shapes can be approximated as circular arcs [22, 26].

As shown in Fig. 2(a), the multiple backbones are routed through the distal segment, curved stem, guiding channels, and proximal segment, with both ends fixed on the end rings of the two continuum segments. The backbone arrangement in the distal segment is proportional to that in the proximal segment, constituting a dual continuum mechanism [20]. Because the total lengths of the backbones are approximately constant, bending of the proximal segment will change the backbones' lengths inside the proximal segment, lending to the backbones' lengths changing inside the distal segment, to bend the distal segment in the opposite direction with a scaled bending angle. Because redundant backbones are arranged in the dual continuum mechanism, thinner backbones can be used to maintain a proper load-bearing capability. At the same time, thinner backbones can lead to larger bending curvature. Within a limited segment length, tight bending (i.e. larger bending angles) can be achieved. Thus, the design of the continuum segment as the distal wrist contributes to the SORST's dexterity and payload capability.

The shape of the curved stem is optimized for increased dexterity. In an SPL setup, if straight-stemmed tools are used, the patient-side extracorporeal manipulators can only swing the tools within limited ranges before mutual collisions occur. With the help of the curved stem, wide-range motions of the patient-side manipulators become possible to enhance the SORST's dexterity. Currently, a two-arc shape of the curved stem is proposed. The stem shape is kinematically optimized as presented in Section 5. The curved stem is

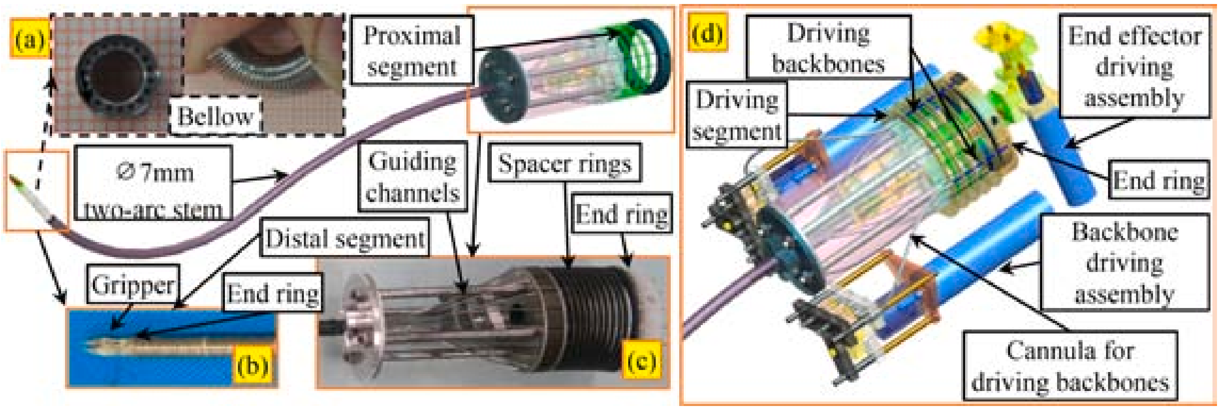

Fig. 2. (a) The proposed SORST tool, (b) the distal segment as a dexterous continuum wrist, with a gripper attached, (c) the proximal segment, and (d) the actuation unit.

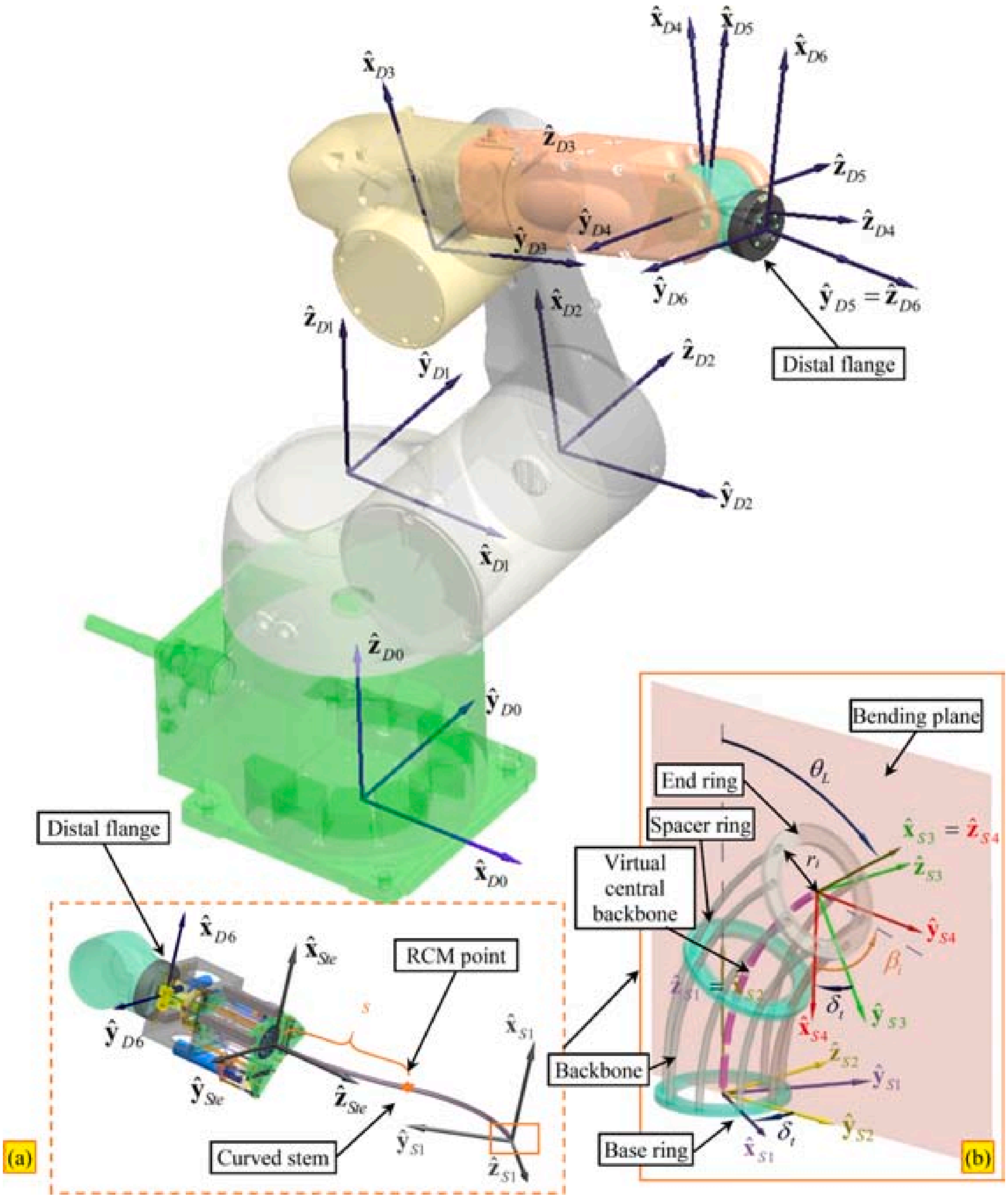

Fig. 3. (a) The Denso-SORST system, and (b) the continuum segment.

constructed to house all guiding channels for the passage of the backbones of the continuum wrist. The stem has an outer diameter of 7 mm because the bellow that is used for the continuum wrist has an outer diameter of 6.35 mm. The 7-mm diameter is small enough to pass a clinically used trocar. The curved shape and rigidity of the stem also contribute to the SORST's dexterity and payload capability.

The SORST is modular and exchangeable: it can be assembled into the actuation unit presented in Section 2.2 to introduce different surgical end effectors. The SORST structure is purely mechanical, which facilitates sterilization.

2.2. *Actuation unit and control infrastructure*

The actuation unit mainly includes one driving segment, two backbone driving assemblies, and one end effector driving assembly. The driving segment is designed to actuate the proximal segment, with the same structure as the continuum segment in Fig. 3(b). The inner diameter of the end ring of the driving segment matches the outer diameter of the proximal segment. After the proximal segment can be assembled inside the driving segment, the push-pull actuation of the four (two pairs) driving backbones will bend the driving segment together with the proximal segment, to drive the distal segment. Each pair of backbones is distributed with a division angle of 180° and is pushed and pulled for the same amount simultaneously by the servo motor in the backbone driving assembly. Because a gripper is assembled in the SORST, the actuation rod for the gripper is driven by the end effector driving assembly, as shown in Fig. 2(d). Clearly, different SORSTs with different distal structure parameters and end effectors can be fitted to the same actuation unit, as long as they have the same-sized proximal segment, leading to a desired actuation modularity feature.

The control infrastructure is designed for teleoperation, controlling the continuum wrist as well as the Denso manipulator. A Phantom Omni device (Sensable Inc.) is connected to a desktop computer to distribute commands from the operator. Details can be found in [27].

3. Kinematics framework

The nomenclature and coordinates are defined in Section 3.1, with the kinematics of a single continuum segment and the manipulator-SORST system presented in Section 3.2 and Section 3.3, respectively.

3.1. *Nomenclature and coordinates*

The coordinates are defined below with the nomenclature listed in Table I and coordinates shown in Fig. 3 to describe the kinematics of the manipulator-SORST system.

- *World Coordinate* $\{W\} \equiv \{\hat{\mathbf{x}}_W, \hat{\mathbf{y}}_W, \hat{\mathbf{z}}_W\}$ is used to describe multiple manipulator-SORST systems for SPL.
- *Denso Coordinates* $\{Dj\} \equiv \{\hat{\mathbf{x}}_{Dj}, \hat{\mathbf{y}}_{Dj}, \hat{\mathbf{z}}_{Dj}\}$ are assigned to the joint axes of the Denso manipulator based on the Denavit-Hartenberg rules, as shown in Table II. $\{D0\}$ is located at the base of the Denso manipulator.
- *Stem Coordinate* $\{Ste\} \equiv \{\hat{\mathbf{x}}_{Ste}, \hat{\mathbf{y}}_{Ste}, \hat{\mathbf{z}}_{Ste}\}$ is translated from $\{D6\}$ by distance l in the $\hat{\mathbf{z}}_{D6}$ direction. $\{Ste\}$ is located at the base of the stem with an optimized two-arc planar curve in the YZ plane.
- *Segment Base Coordinate* $\{S1\} \equiv \{\hat{\mathbf{x}}_{S1}, \hat{\mathbf{y}}_{S1}, \hat{\mathbf{z}}_{S1}\}$ is attached to the segment's base ring. The XY plane is aligned with the base ring with its origin at the center. $\hat{\mathbf{x}}_{S1}$ points from the center to the 1st backbone.
- *Segment Base Bending Coordinate* $\{S2\} \equiv \{\hat{\mathbf{x}}_{S2}, \hat{\mathbf{y}}_{S2}, \hat{\mathbf{z}}_{S2}\}$ is located at $\{S1\}$'s origin with the segment in the XY plane.
- *Segment Tip Bending Coordinate* $\{S3\} \equiv \{\hat{\mathbf{x}}_{S3}, \hat{\mathbf{y}}_{S3}, \hat{\mathbf{z}}_{S3}\}$ is obtained from $\{S2\}$ by a rotation about $\hat{\mathbf{z}}_{S2}$ such that $\hat{\mathbf{x}}_{S3}$ becomes tangent to the virtual central backbone at the end ring. The origin of $\{S3\}$ is at the center of the end ring.
- *Segment Tip Coordinate* $\{S4\} \equiv \{\hat{\mathbf{x}}_{S4}, \hat{\mathbf{y}}_{S4}, \hat{\mathbf{z}}_{S4}\}$ is fixed to the end ring. $\hat{\mathbf{x}}_{S4}$ points from the end ring center to the first backbone. $\hat{\mathbf{z}}_{S4}$ is normal to the end ring.

TABLE I
Nomenclature Used in This Paper

Symbol	Definition
j	Index of the DoFs of the Denso-SORST system, $j = 1, 2, \cdots, 8$.
φ_j	Joint values of the Denso manipulator, $j = 1, 2, \cdots, 6$.
l	Distance between the origin of $\{D6\}$ and $\{Ste\}$.
s	Distance along the curved stem from the origin of the $\{Ste\}$ to the RCM point on the stem.
h	Distance from the origin of $\{Ste\}$ to that of $\{S1\}$ along the curved stem.
h_1, h_2	Length of the first circular arc (near to $\{D6\}$) and the second circular arc of the curved stem, respectively. $h_1 + h_2 = h$.
θ_1, θ_2	Bending angle of the first and second circular arc, respectively.
g	Distance between the gripper tip and the end ring plane.
L	Length of the continuum segment.
θ_L	Right-handed rotation angle about $\hat{\mathbf{z}}_{S2}$ from $\hat{\mathbf{x}}_{S2}$ to $\hat{\mathbf{x}}_{S3}$.
δ	Right-handed rotation angle about $\hat{\mathbf{z}}_{S1}$ from $\hat{\mathbf{y}}_{S2}$ to $\hat{\mathbf{x}}_{S1}$.
$\mathbf{\Psi}_D$	$\mathbf{\Psi}_D \equiv [\varphi_1\ \varphi_2\ \cdots\ \varphi_6]^T$ is the Denso manipulator's configuration vector.
$\mathbf{\Psi}_S$	$\mathbf{\Psi}_S \equiv [\theta_L\ \delta]^T$ is the continuum segment's configuration vector.
$\mathbf{\Psi}$	$\mathbf{\Psi} \equiv [\mathbf{\Psi}_D{}^T\ \mathbf{\Psi}_S{}^T]^T$ is the configuration vector of the Denso-SORST system.
$^{a}\mathbf{p}_{b\_c}$	Position vector from the origin of frame $\{b\}$ to the origin of frame $\{c\}$ in the frame of $\{a\}$.
$^{a}\mathbf{R}_b$	Coordinate transformation matrix from frame $\{b\}$ to frame $\{a\}$.
$^{a}\mathbf{T}_b$	Homogeneous transformation from frame $\{b\}$ to frame $\{a\}$.
$^{a}\mathbf{v}_b$, $^{a}\boldsymbol{\omega}_b$	Linear and angular velocities of frame $\{b\}$ with respect to $\{a\}$.

TABLE II
Structure Parameters and Ranges of the Denso Manipulator with SORST

Denavit-Hartenberg parameters of the Denso manipulator						Structural parameters	
No.	$\alpha_{j\text{-}1}$ (rad)	$a_{j\text{-}1}$ (mm)	d_j (mm)		ξ_j (rad)	l	200 mm
1	0	0	475		φ_1	g	15 mm
2	-π/2	180	0		$\varphi_2-\pi/2$	Optimized results	
3	0	520	0		φ_3	h_1	200 mm
4	-π/2	100	590		φ_4	h_2	200 mm
5	π/2	0	0		φ_5	θ_1	30°
6	-π/2	0	90		φ_6	θ_2	70°
	φ_1	φ_2	φ_3	φ_4	φ_5	φ_6	θ_L
min	-170°	-90°	-168°	-185°	-120°	-360°	0°
max	170°	135°	80°	185°	120°	360°	90°

3.2. *Kinematics of a single continuum segment*

According to the constant bending assumption [22], the center position of the end ring is derived as follows.

$$ {}^{S1}\mathbf{p}_{S1\_S4} = \frac{L}{\theta_L}[\cos\delta(1-\cos\theta_L) \quad \sin\delta(\cos\theta_L-1) \quad \sin\theta_L]^T \tag{1} $$

When θ_L approaches zero, ${}^{S1}\mathbf{p}_{\ S1\_S4} = [0\ 0\ L]^T$.
The orientation mapping from $\{S4\}$ to $\{S1\}$ is as follows.

$$ {}^{S1}\mathbf{R}_{S4} = {}^{S1}\mathbf{R}_{S2}{}^{S2}\mathbf{R}_{S3}{}^{S3}\mathbf{R}_{S4} \tag{2} $$

Where ${}^{S1}\mathbf{R}_{S2} = \mathbf{R}_{\widehat{\mathbf{z}}}(-\delta)\mathbf{R}_{\widehat{\mathbf{x}}}(-\pi/2)\mathbf{R}_{\widehat{\mathbf{z}}}(-\pi/2)$, and $\mathbf{R}_{\widehat{\mathbf{z}}}(-\delta)$ is a simple rotation about $\widehat{\mathbf{z}}$ by an angle $-\delta$. Furthermore, ${}^{S2}\mathbf{R}_{S3} = \mathbf{R}_{\widehat{\mathbf{z}}}(\theta)$, ${}^{S3}\mathbf{R}_{S4} = {}^{S1}\mathbf{R}_{S2}^T$.
The instantaneous kinematics between the configuration space and the task space is as follows.

$$ {}^{S1}\dot{\mathbf{x}}_{S4} = \begin{bmatrix} {}^{S1}\mathbf{v}_{S4}^T & {}^{S1}\boldsymbol{\omega}_{S4}^T \end{bmatrix}^T = \mathbf{J}_S\dot{\boldsymbol{\Psi}}_S = \begin{bmatrix} \mathbf{J}_{vS}^T & \mathbf{J}_{\omega S}^T \end{bmatrix}^T\dot{\boldsymbol{\Psi}}_S \tag{3} $$

Where ${}^{S1}\mathbf{v}_{S4} = \mathbf{J}_{vS}\dot{\boldsymbol{\Psi}}_S$ and ${}^{S1}\boldsymbol{\omega}_{S4} = \mathbf{J}_{\omega S}\dot{\boldsymbol{\Psi}}_S$.
The Jacobian matrix is derived as follows, referring to [22].

$$ \mathbf{J}_{vS} = L\begin{bmatrix} \cos\delta\left(\dfrac{\cos\theta_L-1}{\theta_L^2}+\dfrac{\sin\theta_L}{\theta_L}\right) & \sin\delta\left(\frac{1-\cos\theta_L}{\theta_L^2}-\frac{\sin\theta_L}{\theta_L}\right) & -\frac{\sin\theta_L}{\theta_L^2}+\frac{\cos\theta_L}{\theta_L} \\ \dfrac{\sin\delta}{\theta_L}(\cos\theta_L-1) & \frac{\cos\delta}{\theta_L}(\cos\theta_L-1) & 0 \end{bmatrix}^T \tag{4} $$

$$ \mathbf{J}_{\omega S} = \begin{bmatrix} \sin\delta & \cos\delta & 0 \\ \cos\delta\sin\theta_L & -\sin\delta\sin\theta_L & \cos\theta_L-1 \end{bmatrix}^T \tag{5} $$

3.3. *Kinematics of the manipulator with a SORST*

The Denavit-Hartenberg parameters listed in Table II can be used to describe the kinematics of the Denso manipulator. The homogeneous transformation matrix is as follows.

$$ {}^{D(j-1)}\mathbf{T}_{Dj} = \begin{bmatrix} {}^{D(j-1)}\mathbf{R}_{Dj} & {}^{D(j-1)}\mathbf{p}_{D(j-1)\_Dj} \\ \mathbf{0}_{1\times3} & 1 \end{bmatrix}, \quad j = 1, 2, \cdots, 6 \tag{6} $$

Where ${}^{D(j-1)}\mathbf{R}_{Dj} = \begin{bmatrix} \cos\xi_j & -\sin\xi_j & 0 \\ \sin\xi_j\cos\alpha_{i-1} & \cos\xi_j\cos\alpha_{i-1} & -\sin\alpha_{i-1} \\ \sin\xi_j\sin\alpha_{i-1} & \cos\xi_j\sin\alpha_{i-1} & \cos\alpha_{i-1} \end{bmatrix}$, and ${}^{D(j-1)}\mathbf{p}_{D(j-1)\_Dj} = \begin{bmatrix} a_{j-1} & -d_j\sin\alpha_{i-1} & d_j\cos\alpha_{i-1} \end{bmatrix}^T$.
The Jacobian from $\{D0\}$ to $\{D6\}$ is obtained as follows.

$$ {}^{D0}\dot{\mathbf{x}}_{D6} = \begin{bmatrix} {}^{D0}\mathbf{v}_{D6}^T & {}^{D0}\boldsymbol{\omega}_{D6}^T \end{bmatrix}^T = \mathbf{J}_D\dot{\boldsymbol{\Psi}}_D = \begin{bmatrix} \mathbf{J}_{vD}^T & \mathbf{J}_{\omega D}^T \end{bmatrix}^T\dot{\boldsymbol{\Psi}}_D \tag{7} $$

$$ \mathbf{J}_{vD} = \begin{bmatrix} {}^{D0}\widehat{\mathbf{z}}_{D1}\times{}^{D0}\mathbf{p}_{D1\_D6} & {}^{D0}\widehat{\mathbf{z}}_{D2}\times{}^{D0}\mathbf{p}_{D2\_D6} & {}^{D0}\widehat{\mathbf{z}}_{D3}\times{}^{D0}\mathbf{p}_{D3\_D6} & {}^{D0}\widehat{\mathbf{z}}_{D4}\times{}^{D0}\mathbf{p}_{D4\_D6} & {}^{D0}\widehat{\mathbf{z}}_{D5}\times{}^{D0}\mathbf{p}_{D5\_D6} & \mathbf{0} \end{bmatrix} \tag{8} $$

$$ \mathbf{J}_{\omega D} = \begin{bmatrix} {}^{D0}\widehat{\mathbf{z}}_{D1} & {}^{D0}\widehat{\mathbf{z}}_{D2} & {}^{D0}\widehat{\mathbf{z}}_{D3} & {}^{D0}\widehat{\mathbf{z}}_{D4} & {}^{D0}\widehat{\mathbf{z}}_{D5} & {}^{D0}\widehat{\mathbf{z}}_{D6} \end{bmatrix} \tag{9} $$

The actuation unit and SORST tool are attached to the distal flange of the Denso manipulator, with $\{Ste\}$ translated from $\{D6\}$ by a constant distance of l along $\widehat{\mathbf{z}}_{D6}$: ${}^{D6}\mathbf{p}_{D6\_Ste} = [0\ 0\ l]^T$, ${}^{D6}\mathbf{R}_{Ste} = \mathbf{I}$.

$\{S1\}$ is at a location that is moved from $\{Ste\}$ along a planar curve in the YZ plane of $\{Ste\}$. The transformation involves a simple rotation around $\hat{\mathbf{z}}_{Ste}$, as well as a planar translation, indicated by ${}^{Ste}\mathbf{R}_{S1}$, and ${}^{Ste}\mathbf{p}_{Ste\_S1}$. For the particular case of a straight stem, ${}^{Ste}\mathbf{R}_{S1}$ becomes an identity matrix.

The tip position of the gripper is located at ${}^{S4}\mathbf{p}_{S4\_gp} = [0\ 0\ g]^T$ in $\{S4\}$. The tip position in $\{D0\}$ can be achieved as in (10).

$$ {}^{D0}\mathbf{T}_{\mathrm{gp}} = \left(\prod_{j=1}^{6} {}^{D(j-1)}\mathbf{T}_{Dj} \right) {}^{D6}\mathbf{T}_{Ste}\, {}^{Ste}\mathbf{T}_{S1}\, {}^{S1}\mathbf{T}_{S4}\, {}^{S4}\mathbf{T}_{\mathrm{gp}} \tag{10} $$

Where ${}^{D0}\mathbf{T}_{\mathrm{gp}} = \begin{bmatrix} {}^{D0}\mathbf{R}_{\mathrm{gp}} & {}^{D0}\mathbf{p}_{D0\text{-gp}} \\ \mathbf{0}_{1\times 3} & 1 \end{bmatrix}$.

The twist of the gripper tip can then be derived as in (11).

$$ {}^{D0}\dot{\mathbf{x}}_{\mathrm{gp}} = \left[{}^{D0}\mathbf{v}_{\mathrm{gp}}^{T} \quad {}^{D0}\boldsymbol{\omega}_{\mathrm{gp}}^{T} \right]^{T} = \mathbf{J}_{\mathrm{gp}} \dot{\boldsymbol{\Psi}} = \left[\mathbf{J}_{\mathrm{vgp}}^{T} \quad \mathbf{J}_{\omega\mathrm{gp}}^{T} \right]^{T} \dot{\boldsymbol{\Psi}} \tag{11} $$

Where the linear and angular velocities are obtained as follows.

$$ {}^{D0}\mathbf{v}_{\mathrm{gp}} = \mathbf{J}_{\mathrm{v}D} \dot{\boldsymbol{\Psi}}_{\mathbf{D}} + \left(\mathbf{J}_{\omega D} \dot{\boldsymbol{\Psi}}_{\mathbf{D}} \right) \times {}^{D0}\mathbf{p}_{D6\text{-gp}} + {}^{D0}\mathbf{R}_{S1} \left(\mathbf{J}_{\mathrm{v}S} \dot{\boldsymbol{\Psi}}_{S} + \left(\mathbf{J}_{\omega S} \dot{\boldsymbol{\Psi}}_{S} \right) \times {}^{S1}\mathbf{p}_{S4\text{-gp}} \right) \tag{12} $$

$$ {}^{D0}\boldsymbol{\omega}_{\mathrm{gp}} = \mathbf{J}_{\omega D} \dot{\boldsymbol{\Psi}}_{D} + {}^{D0}\mathbf{R}_{S1} \mathbf{J}_{\omega S} \dot{\boldsymbol{\Psi}}_{S} \tag{13} $$

Where ${}^{D0}\mathbf{R}_{S1} = {}^{D0}\mathbf{R}_{D6}\, {}^{D6}\mathbf{R}_{Ste}\, {}^{Ste}\mathbf{R}_{S1}$, ${}^{D0}\mathbf{p}_{D6\_gp} = {}^{D0}\mathbf{R}_{D6}\, {}^{D6}\mathbf{p}_{D6\_gp}$, and ${}^{S1}\mathbf{p}_{S4\_gp} = {}^{S1}\mathbf{R}_{S4}\, {}^{S4}\mathbf{p}_{S4\_gp}$.

The Jacobian matrices of the Denso-SORST system can hence be derived.

$$ \mathbf{J}_{\mathrm{vgp}} = \left[\mathbf{J}_{\mathrm{v}D} - \left[{}^{D0}\mathbf{p}_{D6\text{-gp}} \right]^{\wedge} \mathbf{J}_{\omega D} \quad {}^{D0}\mathbf{R}_{S1} \left(\mathbf{J}_{\mathrm{v}S} - \left[{}^{S1}\mathbf{p}_{S4\text{-gp}} \right]^{\wedge} \mathbf{J}_{\omega S} \right) \right] \tag{14} $$

$$ \mathbf{J}_{\omega\mathrm{gp}} = \left[\mathbf{J}_{\omega D} \quad {}^{D0}\mathbf{R}_{S1} \mathbf{J}_{\omega S} \right] \tag{15} $$

Where $[\mathbf{p}]^{\wedge}$ is the skew-symmetric matrix of $\mathbf{p}$.

4. Prioritized instantaneous inverse kinematics framework

The proposed instantaneous inverse kinematics framework for the multiple Denso-SORST systems drives the end effector toward the desired twist, while complying with i) the RCM constraint, ii) the mutual collision avoidance constraint, and 3) the joint range/velocity limits.

During teleoperation, the actual RCM point is updated along the curved stem as the projection of the abdominal entry point (i.e.,

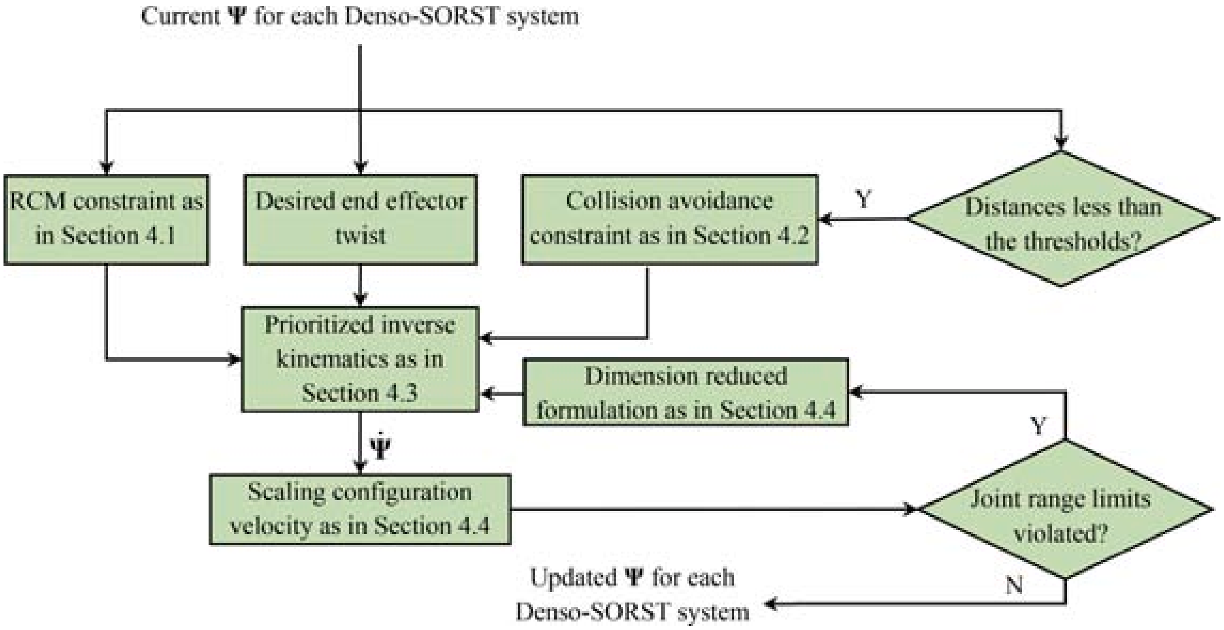

Fig. 4. Flowchart of the prioritized instantaneous inverse kinematics framework.

the desired RCM point). The process of complying with the RCM constraint is defined as minimizing the distance between the projected actual RCM point and the desired RCM point, as in Section 4.1. However, the process of complying with the collision avoidance constraint is defined as increasing the distance between the Denso-SORST entities when the distance is shorter than a preset threshold, as reported in Section 4.2. Because approaching the desired end effector twist should not violate the RCM constraint or the collision avoidance constraint, a prioritized approach is taken, complying with the abovementioned constraints assigned with the highest priority, as presented in Section 4.3. Under the proposed inverse kinematics framework, if the to-be-updated configuration variables and velocities of any of the Denso-SORST systems violate the preset joint ranges or velocity limits, a dimension reduced inverse kinematics formulation combined with a velocity scaling method is adopted as in Section 4.4. The flowchart of the prioritized instantaneous inverse kinematics framework for multiple Denso-SORST systems is illustrated in Fig. 4.

4.1. RCM constraint

To comply with the RCM constraint, the projected actual RCM point on the curved stem should always move toward the abdominal entry.

The projected RCM point is the point on the curved stem with the minimal Euclidian distance to the abdominal entry. In this paper, the curved stem is assumed to possess two circular arcs. The minimum distance and the position of the projected RCM point on the arc can be calculated analytically.

Referring to Fig. 5, in frame $\{Ste\}$, the projected RCM point is ${}^{Ste}\mathbf{p}_{Ste\_\mathrm{RCM}}(s) = [0\ f_y(s)\ f_z(s)]^T$, $s \in [0, h]$. The tangent direction along the curved stem varies at different points. The unit vector for the tangent direction along the projected RCM point is calculated as in (16). The actual linear velocity at the projected RCM point is derived as in (17). Hence, the radial direction velocity is then derived as in (18).

$$ {}^{D0}\widehat{\mathbf{z}}_{\mathrm{RCM}} = {}^{D0}\mathbf{R}_{Ste}\left(\frac{\mathrm{d}\,{}^{Ste}\mathbf{p}_{Ste\_\mathrm{RCM}}(s)}{\mathrm{d}s} \Big/ \left\|\frac{\mathrm{d}\,{}^{Ste}\mathbf{p}_{Ste\_\mathrm{RCM}}(s)}{\mathrm{d}s}\right\|_2\right) \tag{16} $$

$$ {}^{D0}\mathbf{v}_{\mathrm{RCM}} = \mathbf{J}_{\mathrm{v}D}\dot{\boldsymbol{\Psi}}_D + \mathbf{J}_{\omega D}\dot{\boldsymbol{\Psi}}_D \times \left({}^{D0}\mathbf{R}_{D6}\,{}^{D6}\mathbf{p}_{D6\_\mathrm{RCM}}(s)\right) \tag{17} $$

Where ${}^{D6}\mathbf{p}_{D6\_\mathrm{RCM}}(s) = {}^{D6}\mathbf{p}_{D6\_Ste} + {}^{D6}\mathbf{R}_{Ste}\,{}^{Ste}\mathbf{p}_{Ste\_\mathrm{RCM}}(s)$.

$$ {}^{D0}\mathbf{v}_{\mathrm{RCM}\perp} = {}^{D0}\mathbf{v}_{\mathrm{RCM}} - \left({}^{D0}\mathbf{v}_{\mathrm{RCM}}^{T}\,{}^{D0}\widehat{\mathbf{z}}_{\mathrm{RCM}}\right){}^{D0}\widehat{\mathbf{z}}_{\mathrm{RCM}} = \mathbf{J}_{\mathrm{RCM}\perp}\dot{\boldsymbol{\Psi}} \tag{18} $$

Where the Jacobian matrix $\mathbf{J}_{\mathrm{RCM}\perp}$ is in (19).

$$ \mathbf{J}_{\mathrm{RCM}\perp} = \left[\left(\mathbf{I} - {}^{D0}\widehat{\mathbf{z}}_{\mathrm{RCM}}\,{}^{D0}\widehat{\mathbf{z}}_{\mathrm{RCM}}^{T}\right)\left(\mathbf{J}_{\mathrm{v}D} - \left[{}^{D0}\mathbf{R}_{D6}\,{}^{D6}\mathbf{p}_{D6\_\mathrm{RCM}}\right]^{\wedge}\mathbf{J}_{\omega D}\right) \quad \mathbf{0}_{3\times 2}\right] \tag{19} $$

The abdominal entry point ${}^{D0}\mathbf{p}_{D0\_\mathrm{AEP}}$ is a stationary point, set upon the insertion of the SORST tool into an abdomen. The desired converging velocity of the projected RCM point toward ${}^{D0}\mathbf{p}_{D0\_\mathrm{AEP}}$ in the radial direction is set to be proportional to the deviation distance between ${}^{D0}\mathbf{p}_{D0\_\mathrm{AEP}}$ and RCM point ${}^{D0}\mathbf{p}_{D0\_\mathrm{RCM}}(s)$, as in (20).

$$ {}^{D0}\widetilde{\mathbf{v}}_{\mathrm{RCM}\perp} = k_{\mathrm{RCM}}\left({}^{D0}\mathbf{p}_{\mathrm{dis\_RCM}}(s) - \left({}^{D0}\mathbf{p}_{\mathrm{dis\_RCM}}^{T}(s)\,{}^{D0}\widehat{\mathbf{z}}_{\mathrm{RCM}}\right){}^{D0}\widehat{\mathbf{z}}_{\mathrm{RCM}}\right) \tag{20} $$

Where k_{RCM} is a scalar coefficient, ${}^{D0}\mathbf{p}_{\mathrm{dis\_RCM}}(s) = {}^{D0}\mathbf{p}_{D0\_\mathrm{AEP}} - {}^{D0}\mathbf{p}_{D0\_\mathrm{RCM}}(s)$ and ${}^{D0}\mathbf{p}_{D0\_\mathrm{RCM}}(s) = {}^{D0}\mathbf{p}_{D0\_D6} + {}^{D0}\mathbf{R}_{D6}\,{}^{D6}\mathbf{p}_{D6\_\mathrm{RCM}}(s)$.

Mapping the configuration velocities to comply with the RCM constraint for converging the projected RCM point to the abdominal

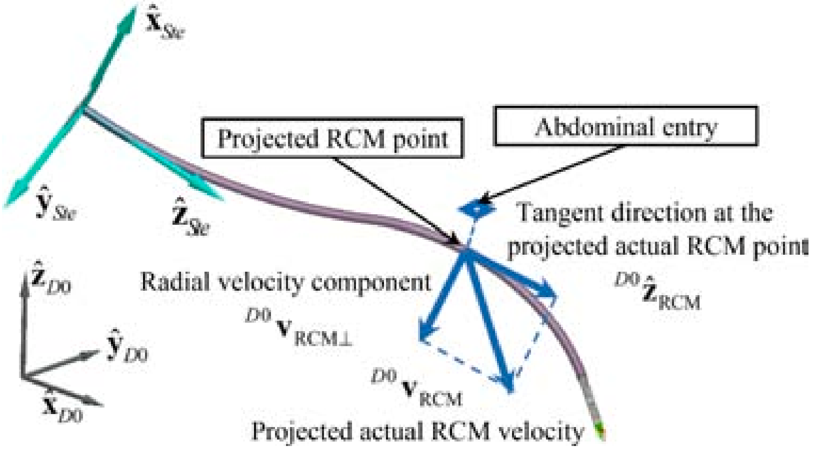

Fig. 5. Velocity decomposition at the projected actual RCM point.

entry is hence defined as in (21).

$$ {}^{D0}\widetilde{\mathbf{v}}_{\mathrm{RCM}\perp} = \mathbf{J}_{\mathrm{RCM}\perp}\dot{\boldsymbol{\Psi}} \tag{21} $$

4.2. *Mutual collision avoidance*

To avoid mutual collisions between the Denso manipulators and the SORSTs inside and outside a patient's abdomen, the separation distance between different entities on the Denso-SORST systems should be quantified. The entities of the Denso manipulators can be simplified as convex polyhedrons, while the SORST can be treated as line segments and circular arcs. The distance between two convex entities can be determined by the GJK algorithm [28], while the distance between line segments can be calculated referring to [29].

For example, two Denso-SORST systems are indicated as A and B. Taking into consideration the SPL deployment as in Fig. 1(d), only the distal links of the Denso manipulator have the risks of mutual collision. As shown in Fig. 10, the link between $\{D3\}$ and $\{D4\}$ is indicated as entity 1, and the structure between $\{D6\}$ and $\{Ste\}$ is indicated as entity 2, with the two circular arcs indicated as entity 3 and entity 4. Four pairs of entities are checked for mutual distances outside the abdomen: A_{e1}-B_{e1}, A_{e1}-B_{e2}, A_{e2}-B_{e1}, and A_{e2}-B_{e2}. Similarly, the entity distances are checked inside the abdomen: A_{e3}-B_{e3}, A_{e3}-B_{e4}, A_{e4}-B_{e3}, and A_{e4}-B_{e4}. These pairs with distances less than the preset threshold are represented by At and Bt ($t = 1,2,3,\ldots$), with the corresponding position vectors of the closest-distanced points on the two entities indicated as $\mathbf{p}_{At}$ and $\mathbf{p}_{Bt}$.

Complying with the collision avoidance constraint is defined as increasing the distance between $\mathbf{p}_{At}$ and $\mathbf{p}_{Bt}$: $d_{t\_AB} = ||\mathbf{p}_{At}$ - $\mathbf{p}_{Bt}||_2$. Hence, the Jacobian matrices, as the partial derivative of the squared distance with respect to $\boldsymbol{\Psi}$, (in forms of row vectors $\mathbf{j}_{At\_\mathrm{ca}}$ and $\mathbf{j}_{Bt\_\mathrm{ca}}$), are in (22).

$$ \begin{cases} \mathbf{j}_{At\_\mathrm{ca}} = \dfrac{\partial d_{t\_AB}^2}{\partial \boldsymbol{\Psi}_A} = 2(\mathbf{p}_{At} - \mathbf{p}_{Bt})^T \dfrac{\partial \mathbf{p}_{At}}{\partial \boldsymbol{\Psi}_A} \\ \mathbf{j}_{Bt\_\mathrm{ca}} = \dfrac{\partial d_{t\_AB}^2}{\partial \boldsymbol{\Psi}_B} = 2(\mathbf{p}_{Bt} - \mathbf{p}_{At})^T \dfrac{\partial \mathbf{p}_{Bt}}{\partial \boldsymbol{\Psi}_B} \end{cases} \tag{22} $$

Where $\boldsymbol{\Psi}_A$ and $\boldsymbol{\Psi}_B$ are the configuration vectors of the two Denso-SORST systems.

The corresponding separating velocities for both $\mathbf{p}_{At}$ and $\mathbf{p}_{Bt}$ are set as in (23).

$$ v_{t\_\mathrm{ca}} = k_{\mathrm{ca}} \big/ \parallel \mathbf{p}_{At} - \mathbf{p}_{Bt} \parallel_2^2 \tag{23} $$

Where k_{ca} is a scalar coefficient for defining the magnitude of the separation velocity.

The entire collision avoidance constraint for multiple pairs of entities whose distance is under the threshold is written in (24).

$$ \begin{cases} \mathbf{v}_{\mathrm{ca}} = \mathbf{J}_{A\_\mathrm{ca}} \dot{\Psi}_A \\ \mathbf{v}_{\mathrm{ca}} = \mathbf{J}_{B\_\mathrm{ca}} \dot{\Psi}_B \end{cases} \tag{24} $$

Where $\dot{\Psi}_A$ and $\dot{\Psi}_B$ are the configuration velocity vectors for the corresponding two Denso-SORST systems A and B, respectively. $\mathbf{J}_{A\_\mathrm{ca}} = [\mathbf{j}_{A1\_\mathrm{ca}}{}^T, \ldots, \mathbf{j}_{At\_\mathrm{ca}}{}^T, \ldots]^T$, $\mathbf{J}_{B\_\mathrm{ca}} = [\mathbf{j}_{B1\_\mathrm{ca}}{}^T, \ldots, \mathbf{j}_{Bt\_\mathrm{ca}}{}^T, \ldots]^T$, $\mathbf{v}_{\mathrm{ca}} = [v_{1\_\mathrm{ca}}, \ldots, v_{t\_\mathrm{ca}}, \ldots]^T$.

4.3. *Prioritized instantaneous inverse kinematics*

The RCM and the collision avoidance constraints should be assigned the highest priority. The end effector is operated under a desired 6-dimensional end-effector twist $\begin{bmatrix} \mathbf{v}_{\mathrm{des}}^T & \boldsymbol{\omega}_{\mathrm{des}}^T \end{bmatrix}^T$. In a surgical procedure, reaching a position is more important than reaching the position with the desired orientation. For example, for a dissection task, reaching the desired dissection point is much more important than reaching the desired end effector orientation. Given that under the RCM and the collision avoidance constraints, the desired end-effector twist may not be fully satisfied, the desired linear velocity ${}^{D0}\mathbf{v}_{\mathrm{des}}$ is set to a higher priority over the desired angular velocity ${}^{D0}\boldsymbol{\omega}_{\mathrm{des}}$.

Referring to [9, 27, 30], three-level prioritized inverse kinematics for each Denso-SORST system is derived as in (25), where the lower priority tasks are accommodated with the residual movement capabilities of the system and without violating the higher priority tasks (namely, the constraints).

$$ \dot{\Psi} = \mathbf{J}_{1\mathrm{st}}^{\dagger}\mathbf{v}_{1\mathrm{st}} + \mathbf{J}_{2\mathrm{nd}}^{\dagger}\left(\mathbf{v}_{\mathrm{des}} - \mathbf{J}_{\mathrm{vgp}}\left(\mathbf{J}_{1\mathrm{st}}^{\dagger}\mathbf{v}_{1\mathrm{st}}\right)\right) + \mathbf{J}_{3\mathrm{rd}}^{\dagger}\left(\boldsymbol{\omega}_{\mathrm{des}} - \mathbf{J}_{\omega\mathrm{gp}}\left(\mathbf{J}_{1\mathrm{st}}^{\dagger}\mathbf{v}_{1\mathrm{st}} + \mathbf{J}_{2\mathrm{nd}}^{\dagger}\left(\mathbf{v}_{\mathrm{des}} - \mathbf{J}_{\mathrm{vgp}}\left(\mathbf{J}_{1\mathrm{st}}^{\dagger}\mathbf{v}_{1\mathrm{st}}\right)\right)\right)\right) \tag{25} $$

Where the Jacobian matrices $\mathbf{J}_{1\mathrm{st}} = \begin{bmatrix} \mathbf{J}_{\mathrm{RCM}\perp}^T & \mathbf{J}_{\mathrm{ca}}^T \end{bmatrix}^T$, $\mathbf{J}_{2\mathrm{nd}} = \mathbf{J}_{\mathrm{vgp}}(\mathbf{I} - \mathbf{J}_{1\mathrm{st}}^{\dagger}\mathbf{J}_{1\mathrm{st}})$, and$\mathbf{J}_{3\mathrm{rd}} = \mathbf{J}_{\omega\mathrm{gp}}(\mathbf{I} - \mathbf{J}_{1\mathrm{st}}^{\dagger}\mathbf{J}_{1\mathrm{st}} - \mathbf{J}_{2\mathrm{nd}}^{\dagger}\mathbf{J}_{2\mathrm{nd}})$ are for the RCM and the collision avoidance constraints, for reaching the desired linear velocity, and for reaching the desired angular velocity, respectively. $\mathbf{J}^{\dagger}$ is the Moore-Penrose pseudo-inverse of Jacobian $\mathbf{J}$.

4.4. *Motion capability constraint*

The velocity limit of the j-th element ($\dot{\Psi}|_{j\_\mathrm{lim}}$) is defined in (26), and a scaling-down approach is integrated to avoid excessive joint velocity as in (27).

$$|\dot{\boldsymbol{\Psi}}|_j| \leq \dot{\boldsymbol{\Psi}}|_{j\_\text{lim}} \tag{26}$$

$$\dot{\boldsymbol{\Psi}} = \dot{\boldsymbol{\Psi}} \min_{j=1,2,\cdots,8}\left(|\dot{\boldsymbol{\Psi}}|_{j\_\text{lim}} \Big/ \dot{\boldsymbol{\Psi}}|_j|, 1\right) \tag{27}$$

The lower and upper limits of the *j*-th element of the configuration vector ($\boldsymbol{\Psi}|_{j\_\text{lower}}$ and $\boldsymbol{\Psi}|_{j\_\text{upper}}$) are defined in (28).

$$\boldsymbol{\Psi}|_{j\_\text{lower}} \leq \boldsymbol{\Psi}|_j \leq \boldsymbol{\Psi}|_{j\_\text{upper}} \tag{28}$$

When the updated configuration variables violate the limits, and if they are simply bounded at their limits, this handling may lead to position and/or orientation divergence. Hence, a dimension-reduced approach from [9, 31] is integrated. The fundamental principle lies in reducing the dimension of the Jacobian matrices as formulated in (29), and using the unsaturated joints to satisfy the original tasks and constraints.

$$\mathbf{J}' = \mathbf{J}\mathbf{D} \tag{29}$$

Where **D** is a diagonal matrix, with the *j*-th diagonal elements assigned to 0 when the *j*-th joint's limits are violated; otherwise, it is assigned to 1, representing that the corresponding DoF is available.

The obtained reduced Jacobian matrices will be substituted into (25) to recalculate the configuration vectors. If the updated configuration velocities still lead to the remaining configuration variables violating their limits, then the dimension of the dimension-reduced Jacobian needs to be further reduced as in (29) until all the calculated configuration variables are within their limits.

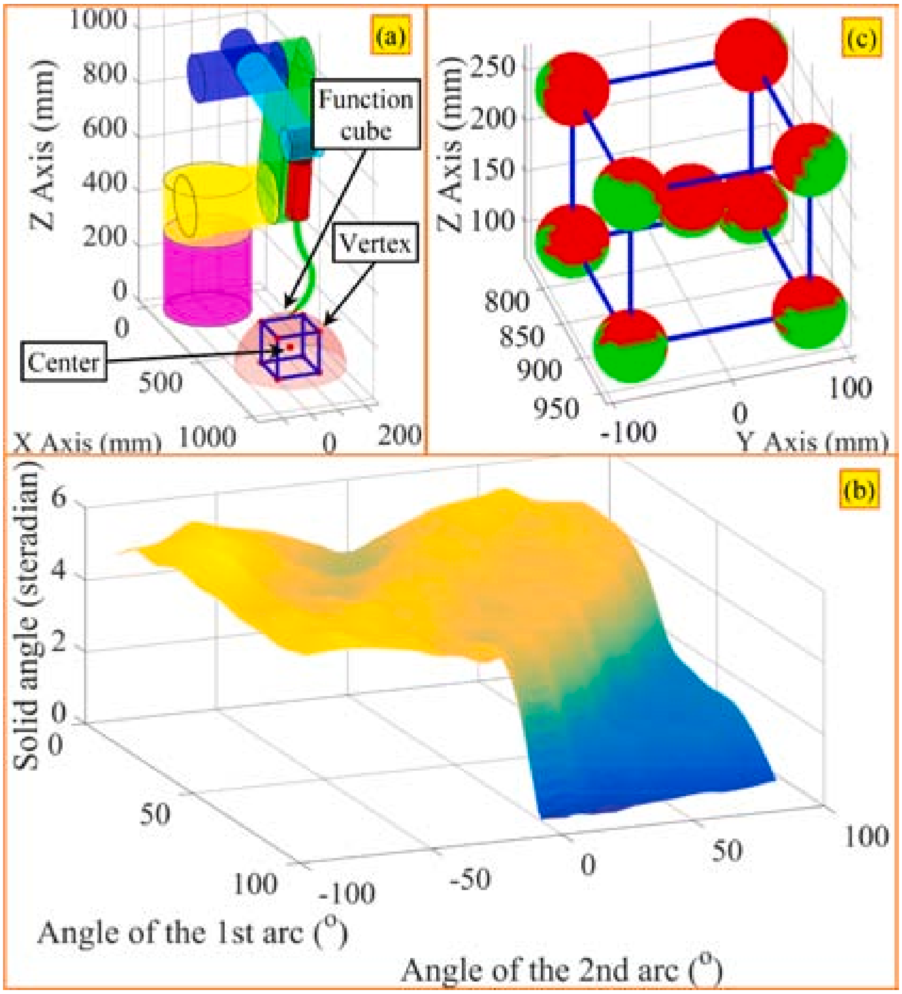

Fig. 6. (a) Deployment of the Denso-SORST system and the cubic functional volume, (b) the optimization results with two 200 mm long arcs, and (c) pointing direction reachability for the optimized configuration, where the green region represents the corresponding pointing direction is reachable.

5. Kinematic optimization for the SORST's curved stem

This section presents the optimization of the stem shape toward better kinematic performance. Since surgical robots are designed toward dexterous movements within a confined surgical site, according to [32], the kinematic performance is then evaluated as the solid angles swept by the end effector axis at selected points. These selected points are the central point and the vertices of a cubic functional volume fitted in the translational workspace as illustrated in Fig. 6(a). The swept solid angles indicate how dexterous the end effectors can be oriented at the center and the vertices of the functional volume.

The stem's shape is structured by two connected arcs and the structural parameters of the curved stem involve the lengths and bending angles of the two arcs. The optimization is conducted in an enumerative manner. Details are reported as follows.

- The stem's total length is set to 400 mm. The length of the first arc (close to the origin of $\{Ste\}$) is enumerated as 100 mm, 200 mm, and 300 mm.
- The shape is bent within the YZ plane in $\{Ste\}$. The bending angle of the first arc varies from 0° to 90° with an increment of 10°. The bending angle in the second arc varies from $-90°$ to 90° with an increment of 10°.
- The patient's abdominal cavity is considered a hemisphere, as shown in Fig. 6(a). The center of the hemisphere is placed right below $\{S6\}$ when the first four joints of the Denso manipulator are set as zero since, at this configuration, the joints of the manipulator are around its range center. The abdominal entry point which is assumed to be at the top of the hemisphere, is treated as the umbilicus in a procedure.
- To test the dexterity at several points, referring to [20, 27, 32], a functional cube with an edge length of 150 mm is defined, which is placed in the symmetry plane of the Denso manipulator and the mockup hemisphere, with the bottom plane coinciding with the bottom of the hemisphere.
- Verifying whether a pointing direction at a selected point is reachable is obtained by verifying whether the inverse kinematics under the RCM constraint has a solution. If a solution exists, the corresponding pointing direction is considered reachable. Furthermore, since the initial configuration also influences the convergence, inverse kinematics is initialized from several poses to first lead the end effector tip to the abdominal entry, as shown in Fig.6(a). Then, inverse kinematics under the RCM constraint, as presented in Section 4, is triggered to converge to the selected points and pointing directions.

The optimized result is 200 mm in length for each arc, as shown in Fig. 6(b), with the Z-axis indicating the average solid angle of the center point and the eight vertices. The maximal average solid angle appears at 30° and $-70°$ for the two arcs. The dexterity sphere is introduced to indicate the pointing direction reachability at a certain point, with the sphere center located at the selected point, and the sphere's radial direction representing the corresponding pointing direction of the end effector. The spheres of the center and the eight vertices in the optimized configuration are illustrated in Fig. 6(c).

6. Experimental characterization

With motion calibration and actuation compensation results in Section 6.1, experiments were conducted to demonstrate the performances of the manipulator-SORST in Section 6.2 and Section 6.3. Section 6.4 illustrates the numerical simulation of SPL deployment with collision avoidance.

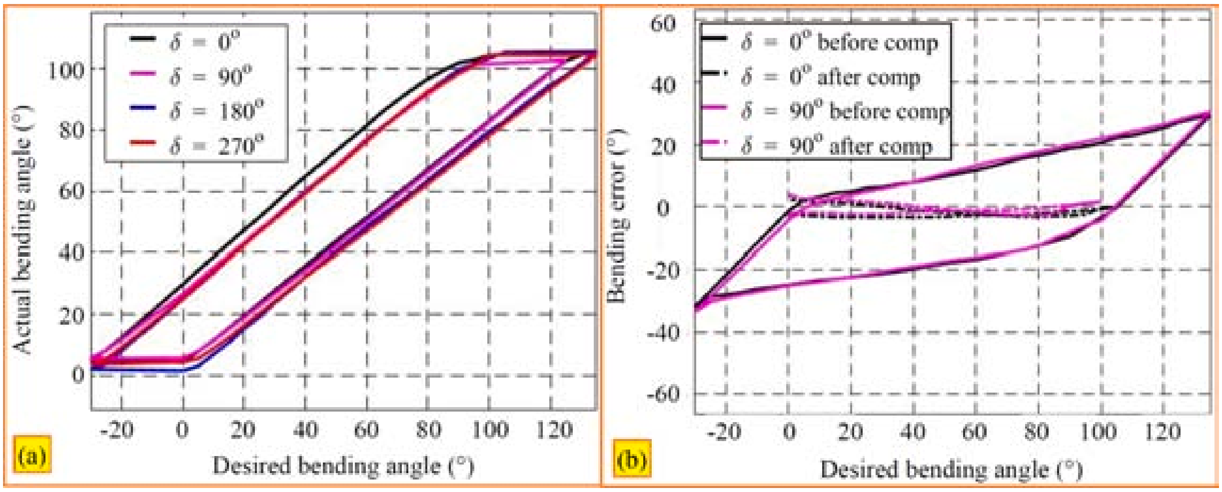

Fig. 7. (a) Motion calibration of the SORST's continuum wrist, and (b) errors before and after compensation.

6.1. Motion calibration and actuation compensation

The continuum segment usually bends less than the desired angle, even though the bent shape can still be approximated as a circular arc. Hence actuation compensation should be formulated based on a bending calibration. Since the process and calculation are the same as those in the existing study in [27], the details are omitted for the sake of brevity.

The desired and actual bending angles before compensation are plotted in Fig. 7(a), with the bending errors before and after compensation plotted in Fig. 7(b). The backlash parameters for the first and second backbone driving assemblies are 1.527 mm and 1.440 mm, respectively. The actuation compensation coefficients for the first and second backbone driving assemblies are 1.241 and 1.266, respectively.

6.2. Constrained motions of the manipulator-SORST

The manipulator-SORST was planned to move along the edges of the functional volume (as defined in Section 5.2) to demonstrate its positioning accuracy under the RCM constraint, using a similar experimental setup as in [27].

The theoretical trajectory and the actual trajectory along with the functional volume are plotted in Fig. 8(a). The average tracking error is 4.36 mm with the largest error of 8.28 mm. During this process, the average error of the RCM point from the abdominal entry point is 3.71 mm with the largest error of 6.64 mm, as shown in Fig. 8(b). The motion errors can be caused by the angular misalignment between $\hat{\mathbf{z}}_{D6}$ and $\hat{\mathbf{z}}_{Ste}$. Such misalignment of 1° may correspond to a position deviation of approximately 9 mm, due to the length of the stem. Another possible reason is the manufacturing error in the shape of the stem.

Although these errors are not negligible, since the manipulator-SORST will be teleoperated in a vision-guided procedure, the errors may be actively corrected by a human operator in the loop.

6.3. Task demonstrations

The manipulator-SORST was teleoperated to complete typical surgical tasks, such as peeling a grape as in Fig. 9(a), transferring pegs as in Fig. 9(b), as well as suturing as in Fig. 9(c).

The teleoperation of the manipulator-SORST is initiated by setting the continuum wrist to be straight. The Denso manipulator is then commanded to insert the wrist through a trocar using the teaching panel. The insertion should continue until the origin of $\{S1\}$ is located at the abdominal entry point (i.e., the distal continuum segment's base ring is aligned with the abdominal entry). The teleoperation starts subsequently according to the kinematics as derived in Section 4.

In the suturing task in Fig. 9(c), the gripper first gripped the tail of the suture and then positioned the tip to the insertion point as well as adjusted the suture's orientation. During the penetration process, the gripper was teleoperated to rotate around the central axis of the suture. After the tip of the suture came out from the other side of the tissue, the gripper released the suture tail and gripped the tip to pull out the suture from the tissue.

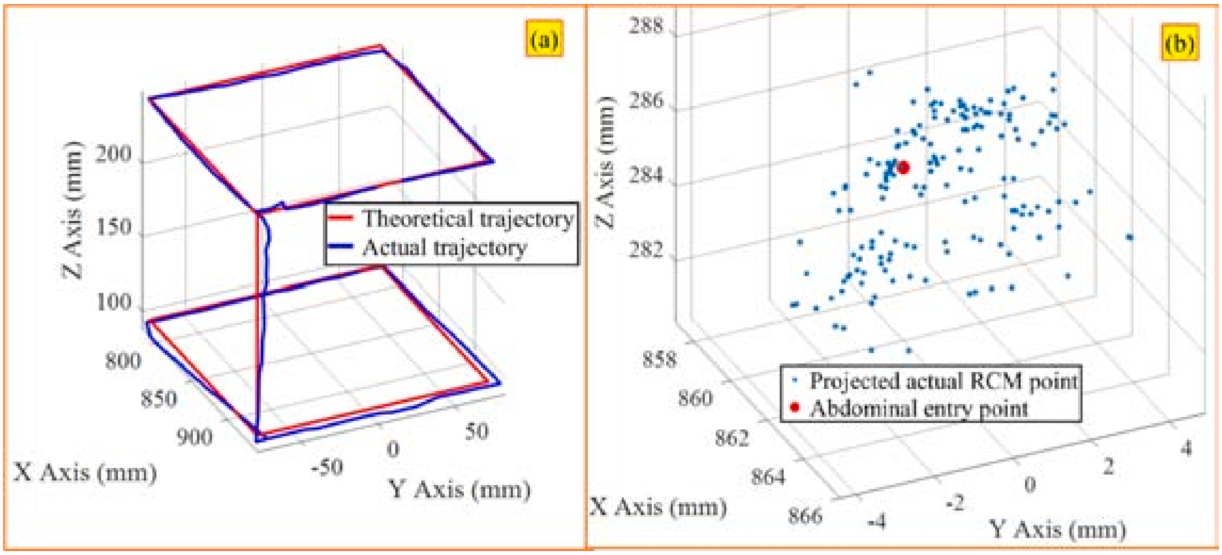

Fig. 8. Movement error quantifications: (a) positioning errors at the gripper tip while scanning the functional volume, (b) the tracked RCM positions.

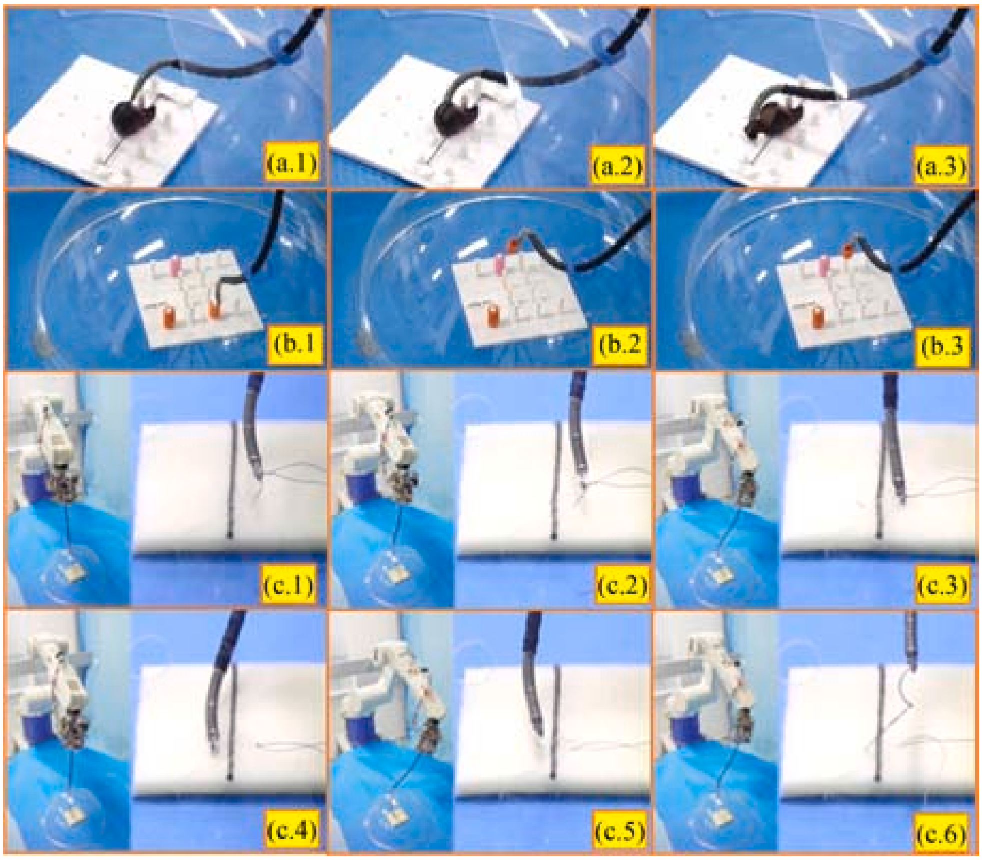

Fig. 9. Teleoperation task demonstrations under the RCM constraint: (a) grape peeling, (b) peg transferring, and (c) suture penetration on a mockup tissue.

6.4. *Numerical experiments for SPL deployment with collision avoidance*

Two Denso-SORST systems (indicated by #1 and #2) are deployed as shown in Fig. 10, and #V represents a Denso manipulator with a straight vision module at the tip. The potential mutual collision risks are detected between the distal two links (entity 1 and entity 2) of the three Denso manipulators outside the abdomen, as well as between the curved stems (two circular arcs as entity 3 and entity 4) inside the abdomen (including the straight vision module). The preset thresholds are 20 mm and 2 mm for the cases outside and inside the abdomen, respectively.

During the simulation, the #V Denso manipulator is not activated, while the two SORST tools' tips of #1 and #2 are instructed to keep the initial orientation and move along a 75×150 mm horizontal rectangle. Fig. 11 shows the eight joint values (including two configuration variables for the continuum wrist) of the two Denso-SORST systems via the proposed prioritized instantaneous inverse kinematics framework. The proposed methods can limit the lateral displacement of the RCM point with respect to the abdominal entry point, as well as keep the position error within a preset threshold (0.01 mm), even when a certain configuration variable violates its limit, as shown in the plots for Joint7 (θ) in Fig. 11. Furthermore, the collision avoidance is well satisfied as the distances are kept above the thresholds, as shown in Fig. 12.

7. Conclusion

This study proposes a robotic surgical tool with a kinematically optimized curved stem and a continuum wrist, and a corresponding collision avoidance inverse kinematics framework, with experimental characterizations and numerical simulations verifying the effectiveness.

The manipulator-SORST makes full use of the advantages of each component: the rigid stem for adequate position accuracy and payload capability, and the continuum mechanism as a wrist for distal dexterity. To further improve the dexterity in a confined surgical site, instead of using a straight stem, a planar two-arc stem is proposed. Besides, the whole manipulator-SORST also supports applicable sterilization and actuation modularity.

The optimization process for the shape of the curved stem is presented to show improved kinematic performance. Correspondingly, to avoid possible collisions, a prioritized inverse kinematics framework is proposed for multiple manipulator-SORST systems to handle

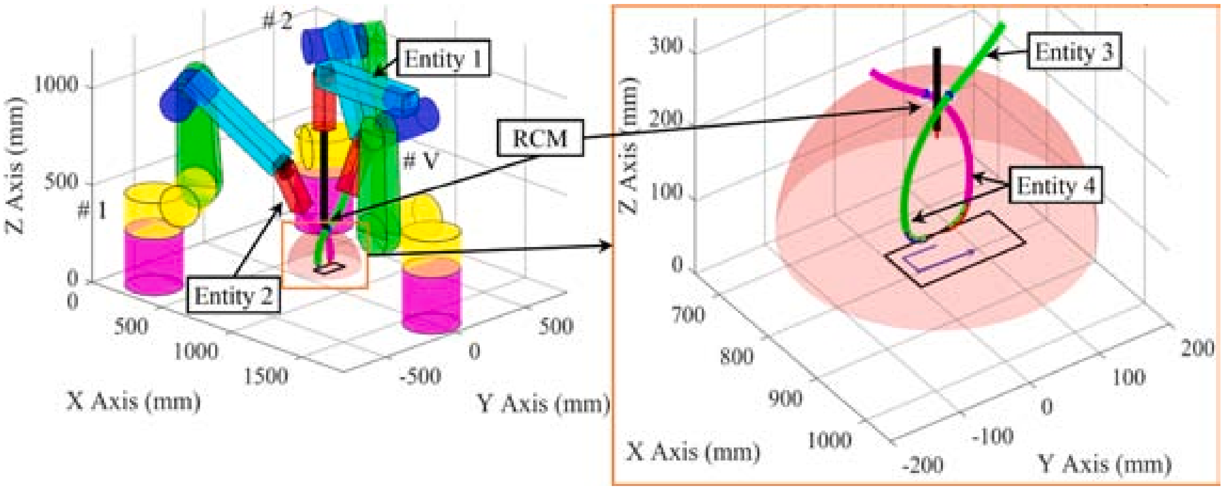

Fig. 10. SPL deployment simulations with collision avoidance.

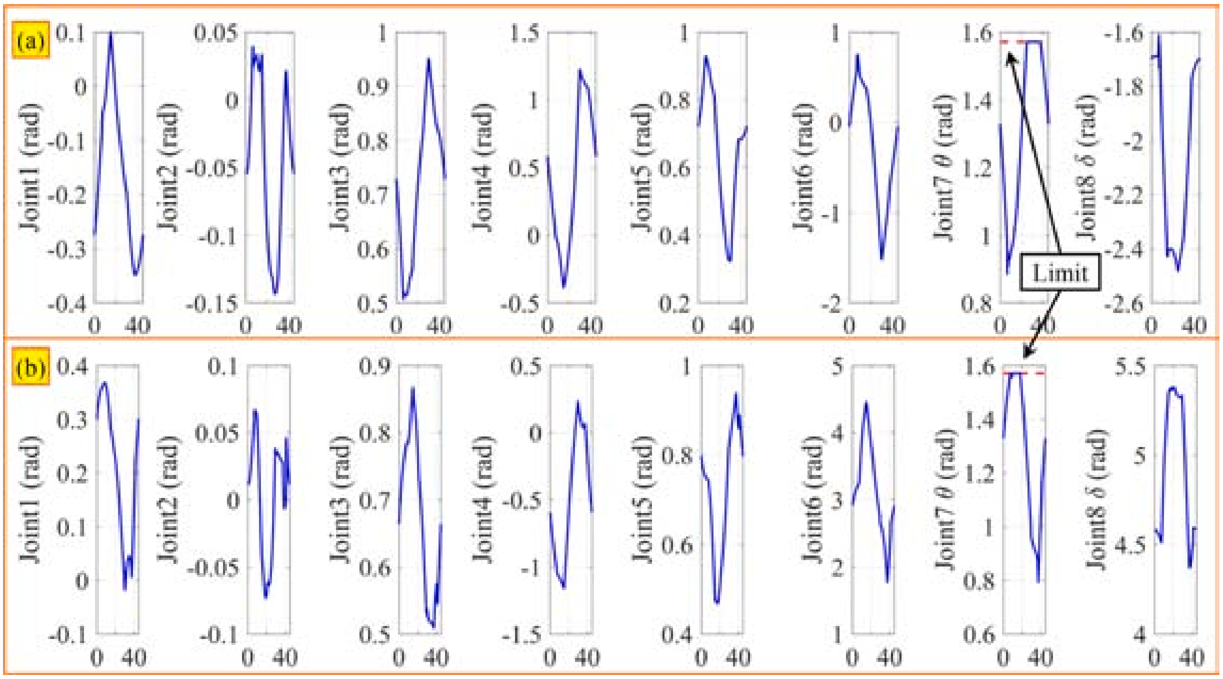

Fig. 11. Eight joint values under the proposed prioritized instantaneous inverse kinematics framework of (a) #1 Denso-SORST, and (b) #2 Denso-SORST. The X-axis represents the elapsed time, with second as the unit.

the desired task space twist, the joint range/velocity limits, the RCM constraint, as well as the mutual collision avoidance constraint.

With the motion calibration and actuation compensation results, the manipulator-SORST was teleoperated to perform typical laparoscopic tasks, such as tissue peeling, peg transferring, and suturing. The movement accuracy of the manipulator-SORST was experimentally quantified. Numerical experiments under an SPL deployment were also conducted to demonstrate the strengths of the proposed instantaneous inverse kinematics, especially in preventing mutual collisions and limiting position deviation.

The design of the manipulator-SORST system can provide an alternative approach to the SPL paradigm. By switching the modular SORST tools, the manipulator-SORST systems can accommodate both single-port and multi-port paradigms. Hence, future efforts will primarily focus on integrating other surgical end effectors and conducting animal studies to further verify the efficacy of the proposed idea.

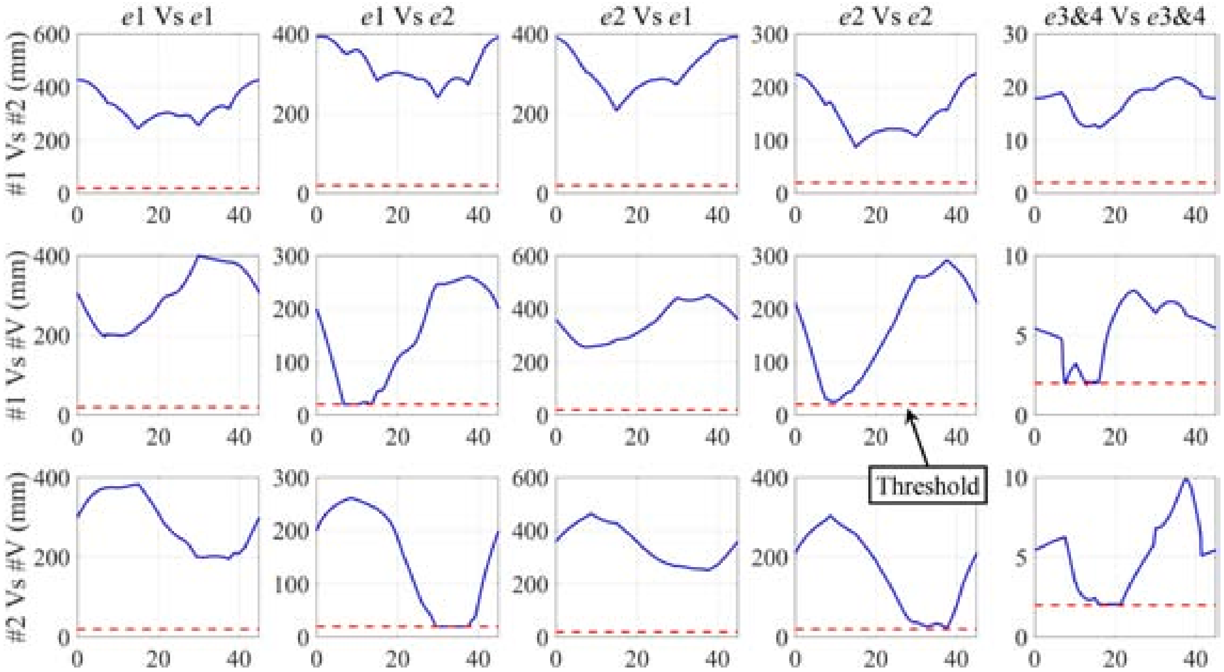

Fig. 12. Distances between the entities of the three manipulators and curved stems (the vision module is treated as a line segment.). The X-axis represents the elapsed time, with second as the unit.

Declaration of Competing Interest

The authors declare that they have no known competing financial interests or personal relationships that could have appeared to influence the work reported in this paper.

Acknowledgments

This work was supported in part by the National Key R&D Program of China (Grant No. 2019YFC0118003, Grant No. 2017YFC0110800 and Grant No. 2019YFC0118004), and in part by the National Natural Science Foundation of China (Grant No. 51722507).

Supplementary materials

Supplementary material associated with this article can be found, in the online version, at doi:10.1016/j.mechmachtheory.2022.104863.

References

[1] Y. Chen, S.a. Zhang, Z. Wu, B. Yang, Q. Luo, K. Xu, A Review of Surgical Robotic Systems for Keyhole and Endoscopic Procedures: State of the Art and Perspectives, Frontiers of Medicine 14 (2020) 382–403.
[2] R.H. Taylor, A Perspective on Medical Robotics, Proc. IEEE 94 (2006) 1652–1664.
[3] T. Kanno, D. Haraguchi, M. Yamamoto, K. Tadano, K. Kawashima, A Forceps Manipulator With Flexible 4-DOF Mechanism for Laparoscopic Surgery, IEEE/ASME Trans. Mechatron. 20 (2015) 1170–1178.
[4] K. Xu, N. Simaan, An Investigation of the Intrinsic Force Sensing Capabilities of Continuum Robots, IEEE Trans. Rob. 24 (2008) 576–587.
[5] U. Kim, D.-H. Lee, Y.B. Kim, D.-Y. Seok, J. So, H.R. Choi, S-Surge: Novel Portable Surgical Robot with Multiaxis Force-Sensing Capability for Minimally Invasive Surgery, IEEE/ASME Trans. Mechatron. 22 (2017) 1717–1727.
[6] H. Azimian, R.V. Patel, M.D. Naish, On Constrained Manipulation in Robotics-Assisted Minimally Invasive Surgery, IEEE /RAS-EMBS International Conference on Biomedical Robotics and Biomechatronics (BIOROB), Tokyo, Japan (2010) 650–655.
[7] E. Lopez, K.-W. Kwok, C.J. Payne, P. Giataganas, G.-Z. Yang, Implicit Active Constraints for Robot-Assisted Arthroscopy, IEEE International Conference on Robotics and Automation (ICRA), Karlsruhe, Germany (2013) 5390–5395.
[8] M.A. Nasseri, P. Gschirr, M. Eder, S. Nair, K. Kobuch, M. Maier, D. Zapp, C. Lohmann, A. Knoll, Virtual Fixture Control of a Hybrid Parallel-Serial Robot for Assisting Ophthalmic Surgery: an Experimental Study, IEEE /RAS-EMBS International Conference on Biomedical Robotics and Biomechatronics (BIOROB), São Paulo, Brazil (2014) 732–738.
[9] F. Flacco, A. De Luca, O. Khatib, Control of Redundant Robots Under Hard Joint Constraints: Saturation in the Null Space, IEEE Trans. Rob. 31 (2015) 637–654.

[10] L. Adhami, E. Coste-Maniere, Optimal Planning for Minimally Invasive Surgical Robots, IEEE Transactions on Robotics and Automation 19 (2003) 854–863.

[11] J.W. Cannon, J.A. Stoll, S.D. Selha, P.E. Dupont, R.D. Howe, D.F. Torchiana, Port Placement Planning in Robot-Assisted Coronary Artery Bypass, IEEE Transactions on Robotics and Automation 19 (2003) 912–917.

[12] A.L. Trejos, R.V. Patel, I. Ross, B. Kiaii, Optimizing Port Placement for Robot-Assisted Minimally Invasive Cardiac Surgery, Int. J. Med. Rob. Comput. Assisted Surg. 3 (2007) 355–364.

[13] S. Sabetian, T. Looi, E. Diller, J.M. Drake, Self-Collision Detection and Avoidance for Dual-Arm Concentric Tube Robots, IEEE Robotics and Automation Letters 4 (2019) 1–9.

[14] M.M. Marinho, B.V. Adorno, K. Harada, M. Mitsuishi, Dynamic Active Constraints for Surgical Robots Using Vector-Field Inequalities, IEEE Trans. Rob. 35 (2019) 1166–1185.

[15] A. Banach, K. Leibrandt, M. Grammatikopoulou, G.-Z. Yang, Active Contraints for Tool-Shaft Collision Avoidance in Minimally Invasive Surgery, International Conference on Robotics and Automation (ICRA), Montreal, QC, Canada (2019) 1556–1562.

[16] R. Moccia, C. Iacono, B. Siciliano, F. Ficuciello, Vision-Based Dynamic Virtual Fixtures for Tools Collision Avoidance in Robotic Surgery, IEEE Robotics and Automation Letters 5 (2020) 1650–1655.

[17] B. Seeliger, M. Diana, J.P. Ruurda, K.M. Konstantinidis, J. Marescaux, L.L. Swanström, Enabling Single-Site Laparoscopy: The SPORT Platform, Surg. Endosc. (2019).

[18] T.D. Wortman, J.M. Mondry, S.M. Farritor, D. Oleynikov, Single-Site Colectomy With Miniature In Vivo Robotic Platform, IEEE Trans. Biomed. Eng. 60 (2013) 926–929.

[19] Y. Kobayashi, Y. Sekiguchi, T. Noguchi, Y. Takahashi, Q. Liu, S. Oguri, K. Toyoda, M. Uemura, S. Ieiri, M. Tomikawa, T. Ohdaira, M. Hashizume, M.G. Fujie, Development of a Robotic System with Six-Degrees-of-Freedom Robotic Tool Manipulators for Single-Port Surgery, Int. J. Med. Rob. Comput. Assisted Surg. 11 (2015) 235–246.

[20] K. Xu, J. Zhao, M. Fu, Development of the SJTU Unfoldable Robotic System (SURS) for Single Port Laparoscopy, IEEE/ASME Trans. Mechatron. 20 (2015) 2133–2145.

[21] I.A. Gravagne, C.D. Rahn, I.D. Walker, Large Deflection Dynamics and Control for Planar Continuum Robots, IEEE/ASME Trans. Mechatron. 8 (2003) 299–307.

[22] K. Xu, N. Simaan, Analytic Formulation for the Kinematics, Statics and Shape Restoration of Multibackbone Continuum Robots via Elliptic Integrals, Journal of Mechanisms and Robotics 2 (2010) 1–13.

[23] D.C. Rucker, R.J. Webster, Statics and Dynamics of Continuum Robots With General Tendon Routing and External Loading, IEEE Trans. Rob. 27 (2011) 1033–1044.

[24] W.S. Rone, P. Ben-Tzvi, Continuum Robot Dynamics Utilizing the Principle of Virtual Power, IEEE Trans. Rob. 30 (2014) 275–287.

[25] C. Yang, S. Geng, I.D. Walker, D.T. Branson, J. Liu, J.S. Dai, R. Kang, Geometric Constraint-Based Modeling and Analysis of a Novel Continuum Robot with Shape Memory Alloy Initiated Variable Stiffness, The International Journal of Robotics Research 39 (2020) 1620–1634.

[26] R.J. Webster, B.A. Jones, Design and Kinematic Modeling of Constant Curvature Continuum Robots: A, Review International Journal of Robotics Research 29 (2010) 1661–1683.

[27] Z. Dai, Z. Wu, J. Zhao, K. Xu, A Robotic Laparoscopic Tool with Enhanced Capabilities and Modular Actuation, Sci. China: Technol. Sci. 62 (2019) 47–59.

[28] S. Cameron, Enhancing GJK: Computing Minimum and Penetration Distances between Convex Polyhedra, IEEE International Conference on Robotics and Automation (ICRA), Albuquerque, New Mexico, USA (1997) 3112–3117.

[29] K. Leibrandt, G.-Z. Yang, Efficient Proximity Queries for Continuum Robots on Parallel Computing Hardware, IEEE Robotics and Automation Letters 2 (2017) 1548–1555.

[30] D.N. Nenchev, Restricted Jacobian Matrices of Redundant Manipulators in Constrained Motion Tasks, The International Journal of Robotics Research 11 (1992) 584–597.

[31] Z. Wu, H. Yang, X. Liu, K. Xu, Dimension Reduced Instantaneous Inverse Kinematics for Configuration Variable Limits of Continuum Manipulators, IEEE International Conference on Robotics and Biomimetics (ROBIO), Dali, Yunnan, China (2019) 303–308.

[32] K. Xu, J. Zhao, X. Zheng, Configuration Comparison among Kinematically Optimized Continuum Manipulators for Robotic Surgeries through a Single Access Port, Robotica 33 (2015) 2025–2044.